

Waveguide-Integrated, Plasmonic Enhanced Graphene Photodetectors

Jakob E. Muench,[†] Alfonso Ruocco,[†] Marco A. Giambra,^{‡,§} Vaidotas Miseikis,^{‡,¶,§} Dengke Zhang,[†] Junjia Wang,[†] Hannah F. Y. Watson,[†] Gyeong C. Park,[†] Shahab Akhavan,[†] Vito Sorianello,[‡] Michele Midrio,^{||} Andrea Tomadin,[⊥] Camilla Coletti,^{¶,§} Marco Romagnoli,[‡] Andrea C. Ferrari,^{*,†,§} and Ilya Goykhman[#]

[†]Cambridge Graphene Centre, University of Cambridge, Cambridge CB3 0FA, United Kingdom

[‡]Consorzio Nazionale per le Telecomunicazioni, 56124 Pisa, Italy

[¶]Center for Nanotechnology Innovation @ NEST, Istituto Italiano di Tecnologia, 56127 Pisa, Italy

[§]Graphene Labs, Istituto Italiano di Tecnologia, 16163 Genova, Italy

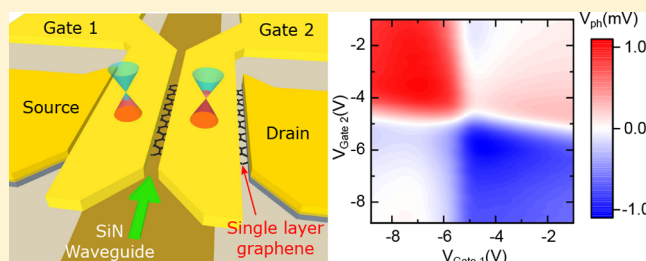
^{||}Consorzio Nazionale per le Telecomunicazioni, University of Udine, 33100 Udine, Italy

[⊥]Dipartimento di Fisica, Università di Pisa, Largo Bruno Pontecorvo 3, 56127 Pisa, Italy

[#]Micro Nanoelectronics Research Center, Technion, Haifa 320000, Israel

ABSTRACT: We present a micrometer-scale, on-chip integrated, plasmonic enhanced graphene photodetector (GPD) for telecom wavelengths operating at zero dark current. The GPD is designed to directly generate a photovoltage by the photothermoelectric effect. It is made of chemical vapor deposited single layer graphene, and has an external responsivity ~ 12.2 V/W with a 3 dB bandwidth ~ 42 GHz. We utilize Au split-gates to electrostatically create a p-n-junction and simultaneously guide a surface plasmon polariton gap-mode. This increases the light–graphene interaction and optical absorption and results in an increased electronic temperature and steeper temperature gradient across the GPD channel. This paves the way to compact, on-chip integrated, power-efficient graphene based photodetectors for receivers in tele- and datacom modules.

KEYWORDS: Graphene, photodetectors, photothermoelectric effect, integrated photonics, plasmonics



The ever-growing demand for global data traffic¹ is driving the development of next-generation communication standards.^{2–4} The increasing numbers of connected devices,⁵ the need for new functionalities, and the development of high-performance computing^{6,7} require optical communication systems and their key building blocks (such as photodetectors (PDs) and modulators) to perform at higher speeds, with improved energy efficiency, while maintaining scalability and cost-effective manufacturing. Si photonics^{8,9} enables dense integration¹⁰ relying on mature, low-cost (based on complementary metal-oxide-semiconductor (CMOS) fabrication processes) manufacturing,^{8,9} making it one of the key technologies for short-reach (<10 km) optical interconnections^{7,11} beyond the currently employed LiNbO₃^{12,13} and InP.^{14,15}

Si photonics-based receivers, where the optical-to-electrical signal conversion is performed, typically employ Ge¹⁶ or bonded III–V PDs,^{17,18} since the photon energies at telecom wavelengths ($\lambda = 1.3–1.6$ μm) are not sufficient for direct (band-to-band) photodetection in Si.¹⁹ In particular, on-chip integrated Ge PDs^{20–24} have matured into standard

components in Si photonics foundries^{8,9,19} and nowadays perform close to their physical limits.⁸ Their external responsivities (in A/W), $R_1 = I_{\text{ph}}/P_{\text{in}}$, where I_{ph} is the photocurrent and P_{in} is the incident optical power, can exceed 1A/W^{8,20} and their bandwidth can reach 60–100 GHz^{22–25} for speed-optimized designs. Following the development of high temperature (>600 °C)¹⁶ heterogeneous integration of Ge-on-Si using epitaxial growth and cyclic thermal annealing,^{16,26,27} the concentration of defects and threading dislocations in Ge epilayers and at Si/Ge interfaces can be reduced,¹⁶ resulting in low (<10 nA^{9,24}) dark current in waveguide integrated Ge p-i-n photodiodes.^{21,24} However, Ge-on-Si integration is complex,^{16,19,27} as the lattice mismatch between Si and Ge,¹⁶ ion implantation,^{20,22} thermal budget (i.e., thermal energy transfer to the wafer) management,¹⁹ and the nonplanarity of Ge layers²⁷ require dedicated solutions during device fabrication.⁹ The charge carrier mobility μ in Si

Received: June 1, 2019

Revised: August 23, 2019

Published: September 19, 2019

and the dislocations and defects in grown¹⁶ or evaporated²⁸ Ge layers set intrinsic limits that prevent further improvements to the operation speed of Ge PDs without compromising R_I .^{9,23} These shortcomings, together with the spectrally limited operation regime (band edge in Ge $\sim 1.57 \mu\text{m}$,¹⁹ which can be extended to $\sim 1.62 \mu\text{m}$ ⁵⁹ at the expense of R_I), and the incompatibility of Ge epitaxy for monolithic integration with other material platforms, such as SiN, are limitations for Ge PDs.^{8,30} Thus, novel solutions for PDs, integrated with Si photonics, at telecom bands are needed.

Graphene is a promising candidate for on-chip integrated photonics.^{31–54} The advantages of single-layer graphene (SLG) stem from its superior optoelectronic properties.⁵⁵ These include high-speed ($>200 \text{ GHz}$ ⁵⁶) operation,⁵⁷ broadband (ultraviolet to far-infrared) absorption,^{58–60} efficient optical modulation (electro-optical index change $\Delta n_{\text{eff}} > 10^{-3}$),³¹ CMOS compatibility,^{41,61} and integrability^{31,62,63} with different on-chip photonics platforms, such as silicon-on-insulator (SOI)³² and SiN.³⁵ In the case of waveguide-integrated graphene PDs (GPDs),^{40–54} high speeds up to 128 GHz,⁴⁹ wafer-scale integration,⁴⁸ and $R_I \sim 0.4\text{--}0.5 \text{ A/W}$ ^{43,37,50,51} were reported. GPDs can offer broadband detection across multiple telecommunication channels (O-band $\sim 1.31 \mu\text{m}$ to U-band $\sim 1.65 \mu\text{m}$),⁴¹ bias-free operation,⁶⁴ and direct generation of photovoltage.^{45,64} This paves the way to GPDs without the noise contribution of dark current^{31,46} and eliminates the need of noise-prone trans-impedance amplifiers (TIA) to convert current to voltage in read-out electronics.³¹

GPDs can be built by exploiting different mechanisms: photovoltaic (PV),^{57,65,66} photothermoelectric (PTE),^{66–68} photogating,⁶⁹ plasma-wave-assisted,⁷⁰ and photobolometric (PB).^{71,72} The dominating effect for a given GPD depends on device configuration, design geometry, and mode of operation.^{66,73} For telecoms, where high-speed (tens GHz) operation is one of the key requirements,^{8,31} PV, PTE, and PB are typically considered for waveguide-integrated GPDs,³¹ exploiting the ultrafast ($\sim \text{fs}$ – ps) carrier dynamics in SLG.^{74,75} Early implementations^{40–42} of this in Si photonics demonstrated $R_I \sim 50\text{--}130 \text{ mA/W}$, predominantly based on PV, with moderate 3 dB roll-off frequency up to $f_{3\text{dB}} \sim 20 \text{ GHz}$.^{40,41} Building on this, subsequent work either optimized individual performance metrics, e.g., $f_{3\text{dB}} \sim 41\text{--}76 \text{ GHz}$ ^{44,48} (with $R_I \sim 1\text{--}7 \text{ mA/W}$ ^{44,48}) or $R_I \sim 0.36\text{--}0.37 \text{ A/W}$ ^{43,47} ($f_{3\text{dB}} \sim 42 \text{ GHz}$ ⁴⁷), or focused on demonstrating integrated GPDs with new waveguide geometries like Si slots⁵³ ($R_I \sim 0.27 \text{ A/W}$), platforms like SiN⁵⁴ ($R_I \sim 15 \text{ mA/W}$, $f_{3\text{dB}} \sim 30 \text{ GHz}$), or scalable fabrication.⁴⁸ The fastest reported, $\sim 110\text{--}128 \text{ GHz}$,^{49–51} on-chip GPDs, with $R_I \sim 0.2\text{--}0.5 \text{ A/W}$,^{49–51} are based on PB and PV. However, these device concepts suffer from unavoidable, typically large ($\sim 100 \mu\text{A}$ ⁵¹), dark currents associated with biasing the SLG channel (e.g., $\sim 0.5 \text{ V}$ ^{49,51}).

PTE is ideal for PD operation in a voltage mode, i.e., with direct read-out of the generated photovoltage. In optically illuminated SLG, electron–electron scattering drives the formation of a “hot” (optically excited) carrier distribution, described by the Fermi–Dirac function,⁷⁶ within $<50 \text{ fs}$.⁷⁴ This can remain at elevated electronic temperatures, T_e , well above the lattice temperature, T_l , over $\sim 2\text{--}4 \text{ ps}$ time scales,⁷⁴ before reaching thermal equilibrium via phonon interaction.^{75,77,78} In this hyperthermal state, a photovoltage V_{ph} is generated by a thermoelectric current as for the Seebeck effect,⁶⁸ if T_e and chemical potential gradients are present in SLG. The sign and

magnitude of V_{ph} depend on the Seebeck coefficient (S), i.e., the proportionality constant between T_e change and photovoltage,⁷⁹ and T_e profile⁶⁸

$$V_{\text{ph}} = \int S(x) \cdot \nabla T_e(x) dx \quad (1)$$

where x is the coordinate along the channel from drain to source, and S is approximated by^{66–68,79}

$$S(x) = -\frac{\pi^2 k_B^2 T_e}{3e} \frac{1}{\sigma(x)} \frac{d\sigma(x)}{d\mu} \quad (2)$$

with $\sigma(x)$ the conductivity, k_B the Boltzmann constant, e the electron charge, and μ_c the chemical potential ($\mu_c = E_F$ at $T_e = 0 \text{ K}$,⁷⁶ with E_F the Fermi energy).

PTE-GPDs have been reported in vertically illuminated^{68,80–83} and waveguide-integrated^{45–47} configurations. The latter used SLG flakes prepared by micromechanical cleavage (MC) of graphite,⁸⁴ with typical device length of tens of μm ,^{45–47} achieving external voltage responsivities, defined as $R_V = V_{\text{ph}}/P_{\text{in}}$, up to $\sim 3.5\text{--}4.7 \text{ V/W}$ ^{45,46} (at zero bias) with speeds $f_{3\text{dB}} \sim 18\text{--}65 \text{ GHz}$.^{45,46} The intrinsic speed limit of PTE-GPDs is related to the cooling time τ_{cooling} of hot electrons in graphene,³¹ which is $\sim 2\text{--}4 \text{ ps}$,⁷⁴ thus limiting the photoswitching rate to $\sim 1/\tau_{\text{cooling}} \sim 250\text{--}500 \text{ GHz}$.⁵⁷ Depending on PTE-GPD design configuration and the requirements of the read-out electronics (i.e., output photo-signal to be measured as current or voltage), the responsivity can be characterized in terms of R_I or R_V . The photovoltage generated by the Seebeck effect is associated with a thermoelectric current across the PD by an Ohmic relation^{45,46,64,81} $I_{\text{ph}} = V_{\text{ph}}/R$, with R the resistance. When operated at zero source-drain bias to function as a photo-generated voltage source, the main contribution to noise in PTE-GPDs comes from thermal (Johnson) noise^{83,85} with $v_n = (4k_B TR)^{1/2}$, where v_n is the root-mean-square noise voltage per hertz of bandwidth in $\text{V Hz}^{-1/2}$. In this case, R becomes a limiting factor for thermal noise and can be reduced, e.g., with high- μ SLG and optimized contact resistance.

To increase R_V for PTE-GPDs, eq 1 suggests two strategies: (1) maximize S ; (2) maximize the T_e gradient profile in the SLG channel. The former increases with increasing μ (see Methods) and decreasing minimum conductivity σ_{min} due to residual charge carriers. Thus, S can be improved by using high- μ SLG, e.g., encapsulating SLG in hBN,^{86–88} using single crystals,^{88,89} or large (tens of μm) domain sizes,⁹⁰ and a transfer process without contamination,^{87,91} strain,⁹¹ or cracks.⁹² Reference 31 suggested that $\mu > 10^4 \text{ cm}^2 \text{ V}^{-1} \text{ s}^{-1}$ could enable $R_V > 100 \text{ V/W}$. The T_e gradient can be increased by creating a localized heat source⁴⁵ generated by enhanced optical absorption in SLG over compact ($<10 \mu\text{m}$) device lengths.^{50,51} This could be achieved by integrating plasmonic nanostructures.^{25,93–97} Subwavelength plasmonic confinement and associated enhancement of the near-field light–matter interaction were previously used to boost the performance of PDs. For example, refs 93 and 94 employed plasmonic structures as Schottky contacts to increase R_I in Si-plasmonic PDs. Ref 25 integrated amorphous Ge with plasmonic slots, reaching internal quantum efficiencies $\sim 36\%$ and high-speed operation $\sim 100 \text{ GHz}$ in the O-band. References 98 and 99 reported microwave detection and mixing based on plasmonic antenna configurations. For PDs based on SLG and other

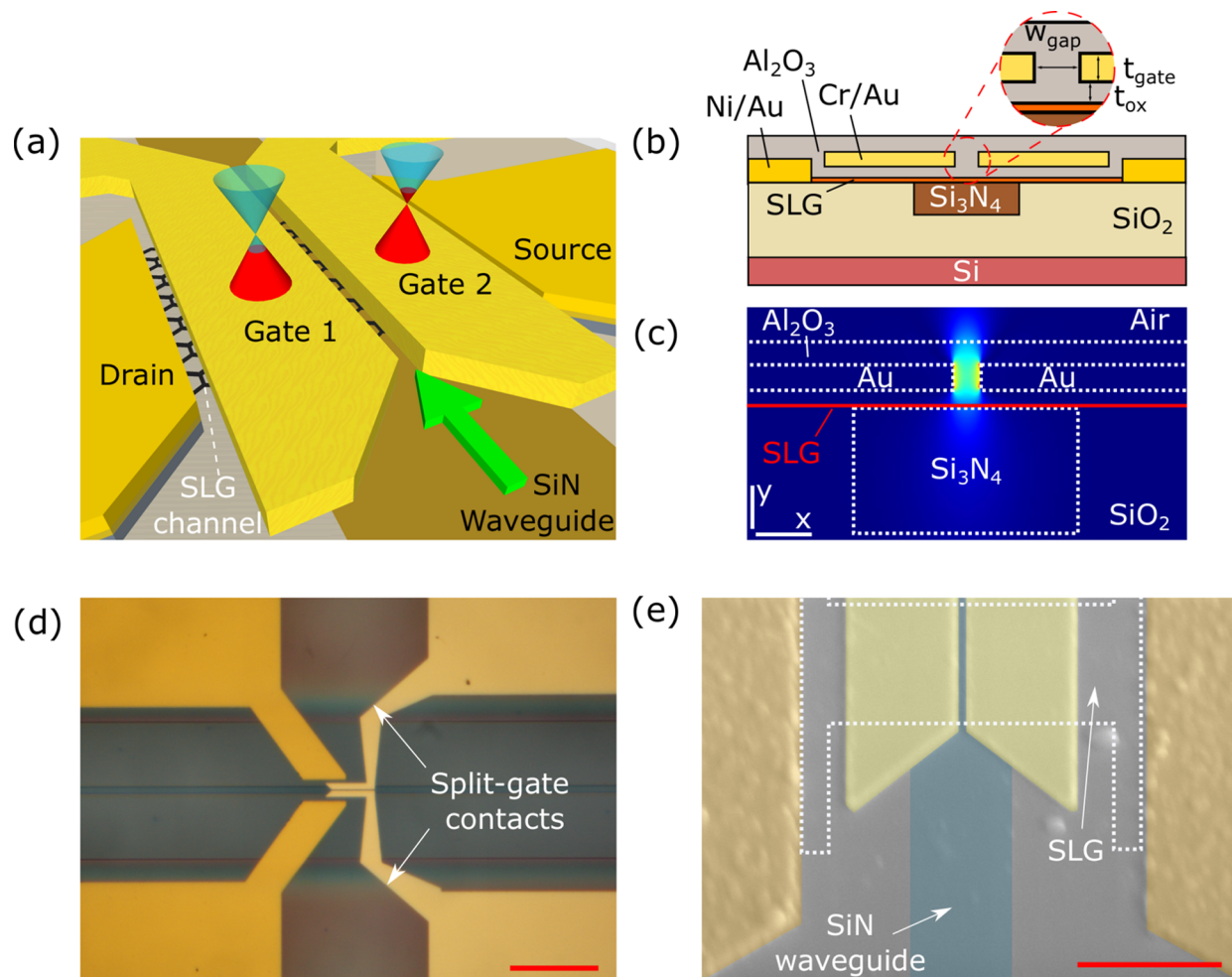


Figure 1. (a) Scheme of our GPD: SLG on SiN waveguide (brown) with split-gates, acting as plasmonic slot waveguide, to create a p–n junction in the channel (as depicted by the Dirac cones above the gates). The green arrow indicates the light propagation direction. (b) Cross section of the GPD active region. (c) Simulated electric field (E_x , in-plane) distribution of the fundamental SPP waveguide mode. For clarity, only the field component parallel to the SLG channel is shown. The vertical and horizontal scale bars are 100 and 250 nm. (d) Optical image of a GPD. Scale bar: 20 μm . (e) Scanning electron micrograph of split-gates. False colors: brown, Ni/Au contacts; yellow, Cr/Au gates; green, planarized SiN waveguide; white dashed line, SLG channel. Scale bar: 2 μm .

layered materials (LMs), the incorporation of plasmonic structures was exploited in free-space^{95–97} and waveguide-integrated^{43,50–52,100} configurations. References 50–52 reported plasmonic-enhanced on-chip GPDs based on PV^{50–52} and PB^{51,52} with $R_I \sim 0.5 \text{ A/W}^{51}$ and bandwidth $\sim 110 \text{ GHz}^{50,51}$ at 1.55 μm for source-drain bias < 1 V.

Here, we report compact ($\sim 0.5\text{--}4 \mu\text{m}$), PTE-based, waveguide-integrated, plasmonic-enhanced GPDs for telecom wavelengths with $R_V \sim 12.2 \text{ V/W}$ at zero source-drain bias and zero dark current, with a 3 dB cutoff frequency $\sim 42 \text{ GHz}$. To the best of our knowledge, this is the largest R_V to date for waveguide-integrated GPDs operating in voltage mode. We use SLG grown by chemical vapor deposition (CVD) and transferred onto low-loss ($\sim 1 \text{ dB/cm}$) planarized (i.e., fully embedded in cladding¹⁰¹) SiN waveguides with a semidry (i.e., combining wet delamination from the growth substrate with dry lamination onto the target substrate) transfer,⁸⁹ unlike previous PTE GPDs exploiting nonscalable MC SLG.^{45,46} Our design relies on Au split-gates to electrostatically create a p–n junction in the SLG channel, as well as to guide a confined SPP waveguide mode. By leveraging optical field enhancement and plasmonic confinement in the gap, we increase the light–SLG

interaction and optical absorption in the p–n junction region, resulting in a confined electron heat source, compact device length, and increased R_V . This combines high-performance (large R_V , high-speed, bias-free, compact, direct V_{ph} read-out) PTE GPDs in the telecom range with scalable fabrication, paving the way for graphene integrated receivers for next-generation transceivers.

The design of our GPD is schematically shown in Figure 1a,b. It comprises a SLG channel on a SiN waveguide supporting a transverse-electric (TE, in-plane) polarized fundamental waveguide mode. Two Au gates are placed above the channel, separated from SLG by an Al_2O_3 spacer and centrally aligned with respect to the waveguide. When this split-gate structure is DC (direct current) biased, it forms a p–n junction (Figure 1a) and creates an S profile in SLG, as in eq 2. When an on-chip guided signal reaches the PD area, it is evanescently coupled from the SiN waveguide to the split-gate, which acts as an SPP waveguide (Figure 1c). The improvement obtained by using plasmonic guidance with light confinement in the gap (width, w_{gap} , $\sim 100 \text{ nm}$) is (1) increased optical field intensity and absorption in SLG and (2) shaping the T_e distribution and its gradient in the channel by

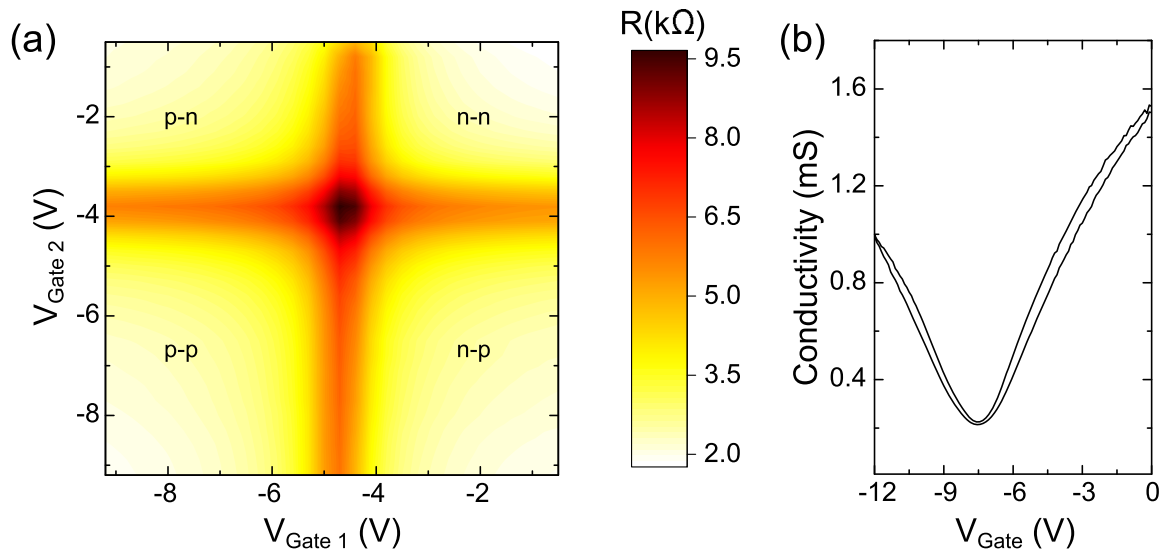


Figure 2. (a) GPD channel resistance as a function of split-gate voltages. (b) Conductivity as a function of gate voltage from a 4-terminal measurement on test Hall bars.

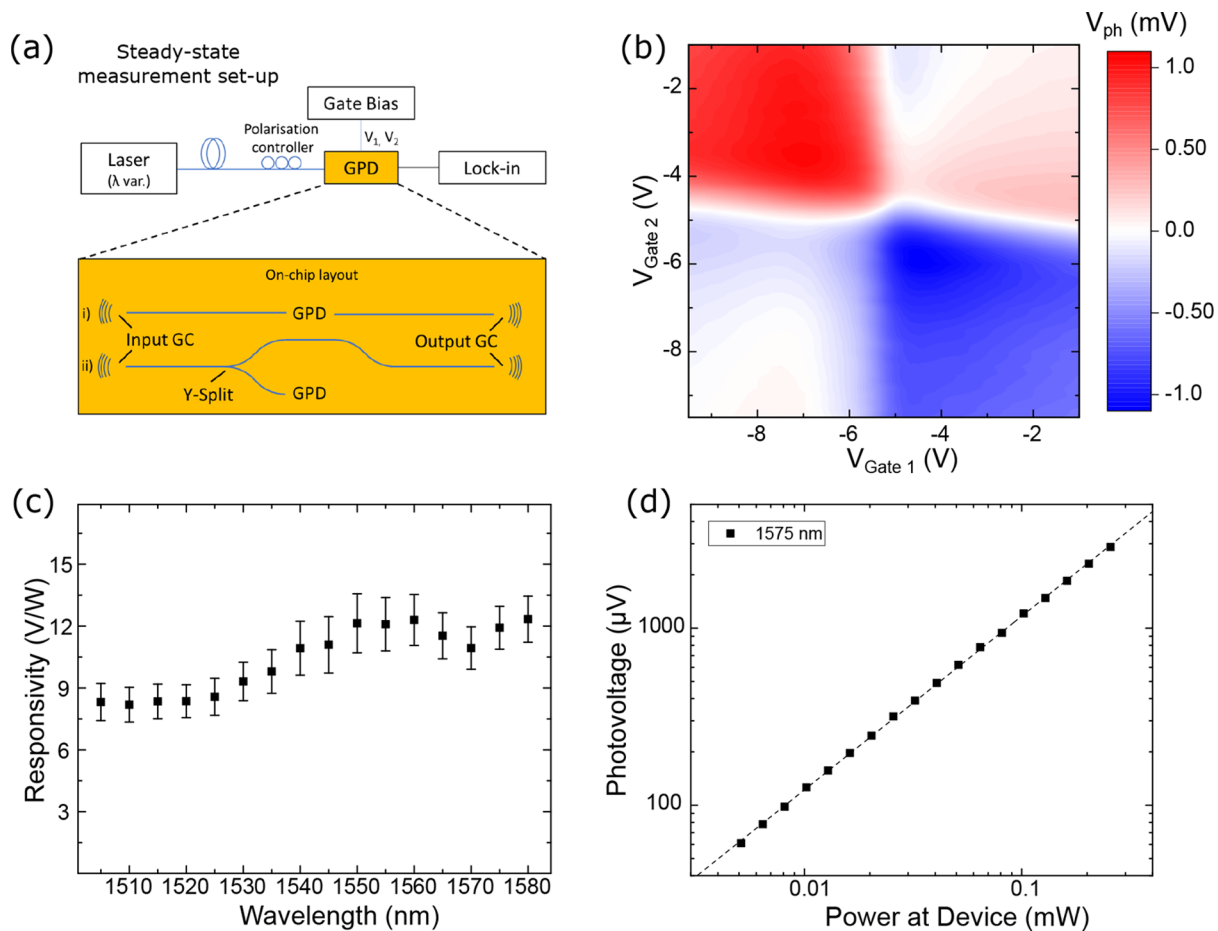


Figure 3. (a) Schematic steady-state photoresponse measurement setup, including on-chip layout with passive photonic structure. GPDs are placed on waveguides (i) without or (ii) with 3 dB Y-splits. (b) Photovoltage map for zero bias. (c) Wavelength dependence and (d) power dependence of responsivity at 1575 nm.

confining the absorption to the narrow region of the slot. The coupling efficiency, P_{out}/P_{in} , where P_{out} is the power transferred between two optical components, from photonic to plasmonic waveguide mode can be optimized by tailoring w_{gap} and dielectric spacer thickness (t_{ox}).

To optimize the cross section parameters at $\lambda = 1.55 \mu\text{m}$, we perform optical simulations using a commercial finite difference solver tool (Lumerical MODE). After selecting the fundamental gap plasmon mode for a given design and λ , we extract the optical electric field distribution in the SLG channel

to model the absorbed power density that generates the hot carrier distribution as time-averaged electric power dissipation density,^{102,103} which we refer to as Joule heat source (J) hereafter. After normalization to an input power of $1 \mu\text{W}$, this is used in the heat equation^{47,67,80}

$$-\kappa_e(x) \left[\frac{d^2}{dx^2} \Delta T_e(x) - \frac{1}{\xi^2} \Delta T_e(x) \right] = J(x) \quad (3)$$

where $\Delta T_e(x) = T_e(x) - T_1$ is the local temperature fluctuation, ξ is the cooling length (see Methods), and $\kappa_e(x)$ is the electronic thermal conductivity (see Methods). Equation 3 gives the $T_e(x)$ profile. Together with the optimum $S(x)$ profile (see Methods), this is used in eq 1 to obtain V_{ph} . The parameters are chosen to maximize V_{ph} .

The fabrication process of the GPDs and a more detailed description of the simulations, including coupling between the dielectric and plasmonic waveguides, and the positioning of the SLG channel along the split-gate are presented in Methods. Figure 1d,e shows images of a representative GPD.

To determine the operating point, we perform electrical characterizations by sweeping the split-gate voltages (V_{Gate1} , V_{Gate2}) while measuring the device current I_{DS} under a constant source-drain bias $V_{\text{DS}} = 1 \text{ mV}$, using DC probes on micromanipulators and two source measurement units. Figure 2a plots the R map of a typical device as a function of V_{Gate1} , V_{Gate2} . This shows a 4-fold pattern, corresponding to the four doping constellations (p-n, n-p, n-n, p-p) for different combinations of gate voltages. The map is symmetric with a maximum $R \sim 9 \text{ k}\Omega$ at the crossing of the charge neutrality point (CNP), between -4 and -5 V . This corresponds to n-doping of the unbiased SLG with $n \sim 7 \times 10^{12} \text{ cm}^{-2}$ ($\sim 350 \text{ meV}$). R has contributions from channel (R_{ch}) and contact (R_{c}) resistances. R_{ch} includes a fixed contribution from ungated SLG regions and a gate-dependent one from channel segments underneath the split-gates. The gate-dependent variation in R in Figure 2a suggests R_{ch} as the dominant factor. This is consistent with our contact resistivity ($< 1 \text{ k}\Omega \mu\text{m}$) for CVD SLG and the calculated R based on channel geometry and sheet resistance obtained from independent four-terminal measurements on reference Hall bars. From these, we also extract an average $\mu \sim 2000 \text{ cm}^2 \text{ V}^{-1} \text{ s}^{-1}$ from linear fits of the conductivity via¹⁰⁴ $\mu = \text{ld}\sigma/dV_{\text{Gate1}}/C_{\text{ox}}$ where C_{ox} is the top gate capacitance. Figure 2b is a bidirectional gate sweep of the conductivity, indicating low hysteresis and charge-trapping in the Au/Al₂O₃/SLG gate capacitor.

To record the static photoresponse (see Figure 3a), we couple continuous-wave (CW) transverse-electric (TE, in-plane) polarized light at $1.50\text{--}1.58 \mu\text{m}$ into the SiN waveguide using a single-mode optical fiber and an input grating coupler (GC). V_{ph} is recorded between source and drain electrodes across the unbiased ($V_{\text{DS}} = 0 \text{ V}$) channel as a function of V_{Gate1} and V_{Gate2} , using a lock-in amplifier under internal modulation (square wave, ON–OFF) of the laser at 200 Hz . To ensure constant P_{in} during the experiment, we monitor the transmission with a second fiber positioned over the output GC and connected to an external InGaAs power meter. GPDs are positioned either on bare waveguides ((i) in Figure 3a) or on one of the branches after a $50\text{--}50 \text{ Y-split}$ ((ii) in Figure 3a).

Figure 3b is a V_{ph} map of a typical device at $P_{\text{in}} \sim 100 \mu\text{W}$ inside the GPD. The plot exhibits a 6-fold pattern with higher response for bipolar (p-n, n-p) junctions and a weaker one with sign-crossing along the diagonal ($V_{\text{Gate1}} = V_{\text{Gate2}}$) for

unipolar (n-n, p-p) junctions. When the GPD is operated at zero V_{DS} , this indicates a PTE-dominated photodetection as the two sign changes in V_{ph} along a single-gate sweep line (e.g., $V_{\text{Gate2}} = \text{const.}$) reflect those of the S gradient across the junction, arising from the non-monotonic dependence of S on μ_c ⁶⁷ (see Methods). Contributions from PV and PB effects, which can be present in SLG,^{45,60,66} are negligible or minor here: for PB, because our devices are operated at zero source-drain bias; for PV, because, if this was the main effect, it would result in only one sign-change in V_{ph} along single-gate sweep lines.⁶⁷ The measured photoresponse is in good agreement with the calculated one (see Methods). Small asymmetries in the measured photoresponse can stem from fabrication-induced asymmetries in gate geometry, doping variations during PD operation, and nonuniform μ across the SLG p–n junction. We observed a similar behavior on >12 devices of different sizes across 5 chips, the shortest being 500 nm in the light propagation direction for a footprint $\sim 3 \mu\text{m}^2$. For all devices, V_{ph} reaches its maximum close to the CNP where S is largest, with a gradual drop-off at higher doping.

To calculate R_V , we first estimate the optical power inside our GPDs by taking into account the following: (a) the combined loss from fiber-to-waveguide coupling and propagation in the Al₂O₃-covered SiN waveguide, from reference measurements on empty waveguides (this combined loss is wavelength-dependent, following the spectral response envelope of the GC, and is $\sim 9.6 \text{ dB}$ at the center wavelength); (b) 3 dB power reduction from the input laser modulation (square wave, ON–OFF) with a 50% duty cycle; (c) 3 dB power splitting in the Y-branches and their $\sim 0.2 \text{ dB}$ losses (when applicable). We get $R_V \sim 12.2 \text{ V/W}$, exceeding the current state-of-the-art⁴⁶ by a factor >2.5 , while maintaining scalability with CVD SLG and bias-free operation. The source-drain zero-bias operation in the photovoltage mode eliminates the noise contribution from the dark current typically observed in PV/PB GPDs^{49–51} and integrated Ge photodiodes.^{21,24} Assuming Johnson noise^{83,85} as being dominant in the absence of applied bias, the measured R and R_V maps give a noise equivalent power^{60,85} $\text{NEP} = v_n/R_V \sim 600\text{--}900 \text{ pW Hz}^{-1/2}$ in the p-n and n-p regions in Figure 3b. This can be improved by minimizing R (e.g., using higher- μ SLG, lower contact resistance) and by further maximizing R_V (e.g., by improving coupling efficiency and overall absorption in SLG). Reducing R to match the 50Ω of conventional read-out electronics would also lower the impedance mismatch and increase the power delivered by the GPDs.

Figure 3c plots the R_V wavelength dependence, showing a broadband ($1.50\text{--}1.58 \mu\text{m}$) photoresponse covering the C-band ($1.53\text{--}1.565 \mu\text{m}$ ¹⁰⁵) and beyond. The error bars indicate variations in the wavelength-dependent coupling loss (thus P_{in}), estimated as the standard deviation from transmission measurements on >10 reference waveguides. We attribute the gradual increase in R_V with wavelength to a combination of increased overlap between slot mode and SLG and improved coupling efficiency from the dielectric to the plasmonic waveguide, due to a reduced mode mismatch between fundamental modes in waveguide and hybrid regions. Figure 3d is the V_{ph} power dependence at $1.575 \mu\text{m}$ for power levels comparable to the typical receiver sensitivities required in short-reach optical links.³¹ The linear response indicates a power-independent R_V in the tested P_{in} range, confirming device operation under the $|\Delta T_e(x)| < T_1$ condition, where the electron heat capacity is constant.⁶⁴

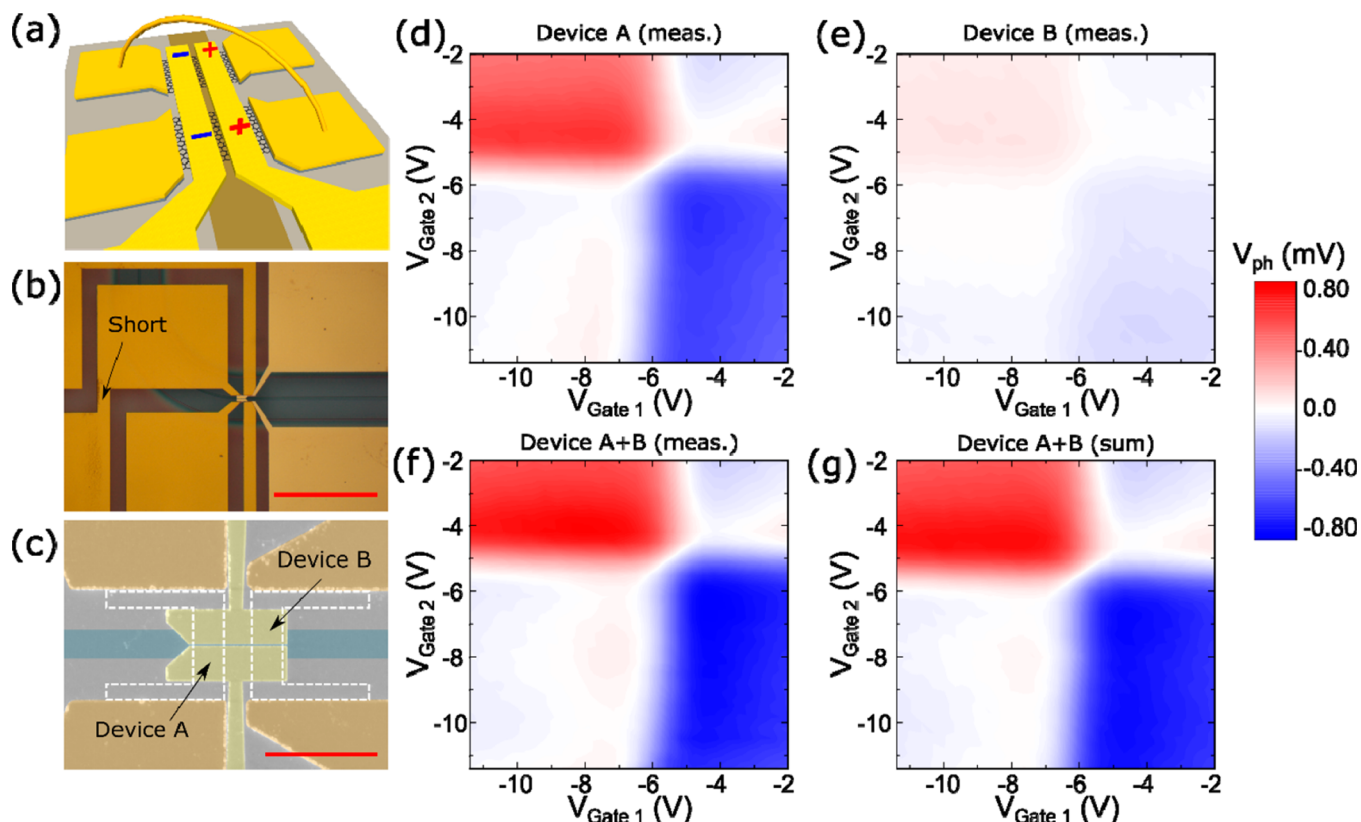


Figure 4. (a) Schematic test structure to measure two GPDs in series. (b) Optical image of contact pad short to connect both GPDs in series. Scale bar: $80\ \mu\text{m}$. (c) SEM image of active region. False colors: brown, Ni/Au contacts; yellow, Cr/Au split gate; green, planarized SiN waveguide. The SLG channels are indicated by white dashed lines. Scale bar: $5\ \mu\text{m}$. (d) Photovoltage map of device A at the start of the SPP waveguide. (e) Photovoltage map of device B at the end of the SPP waveguide. (f) Photovoltage map of devices A, B in series. (g) Sum of A, B photovoltage maps.

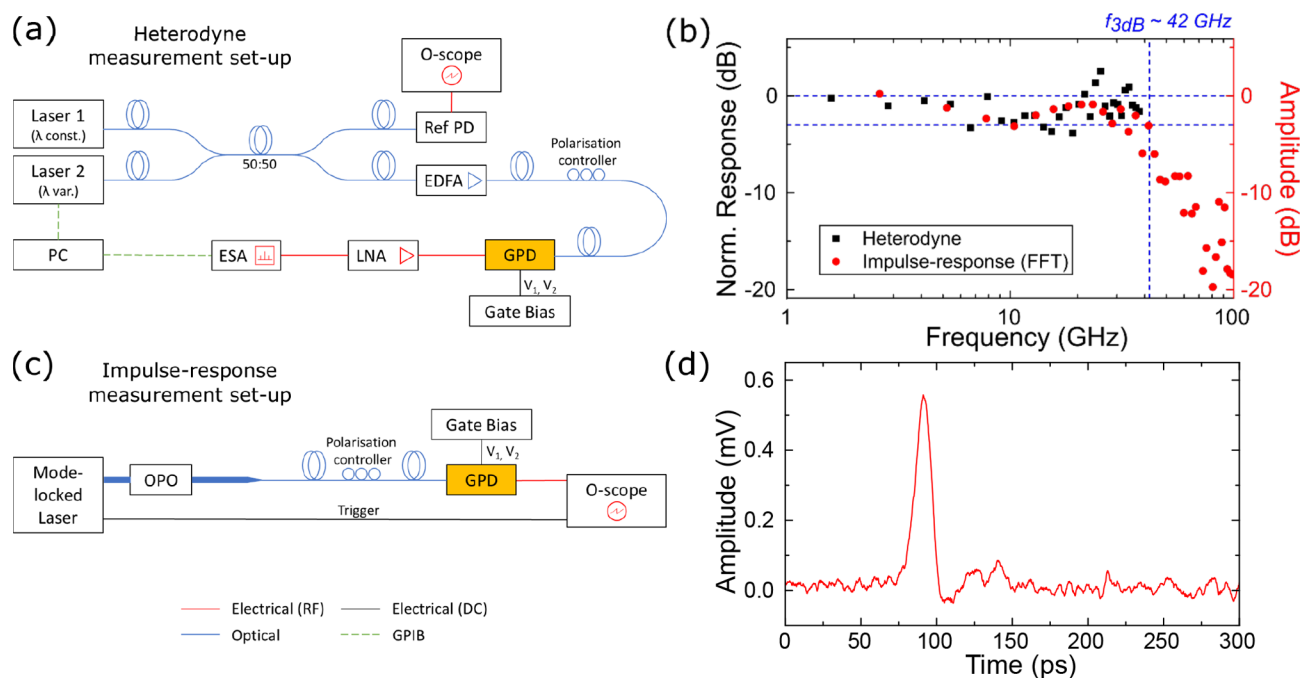


Figure 5. (a) Schematic heterodyne setup. (b) Frequency response at $V_{DS} = 0$ from (black) direct heterodyne measurement and (red) fast Fourier transform of impulse response. (c) Schematic impulse-response setup. (d) Impulse-response for ~ 150 fs pulses at $V_{DS} = 0$ and p-n gate bias.

To highlight our GPDs' behavior as voltage sources, when a signal is generated, we place two devices back to back on the same waveguide and connect them in series. This modified

design (Figure 4a) consists of two SLG channels gated from the same split-gate/SPP waveguide. By connecting the drain pad of one channel to the source of the other through a metal

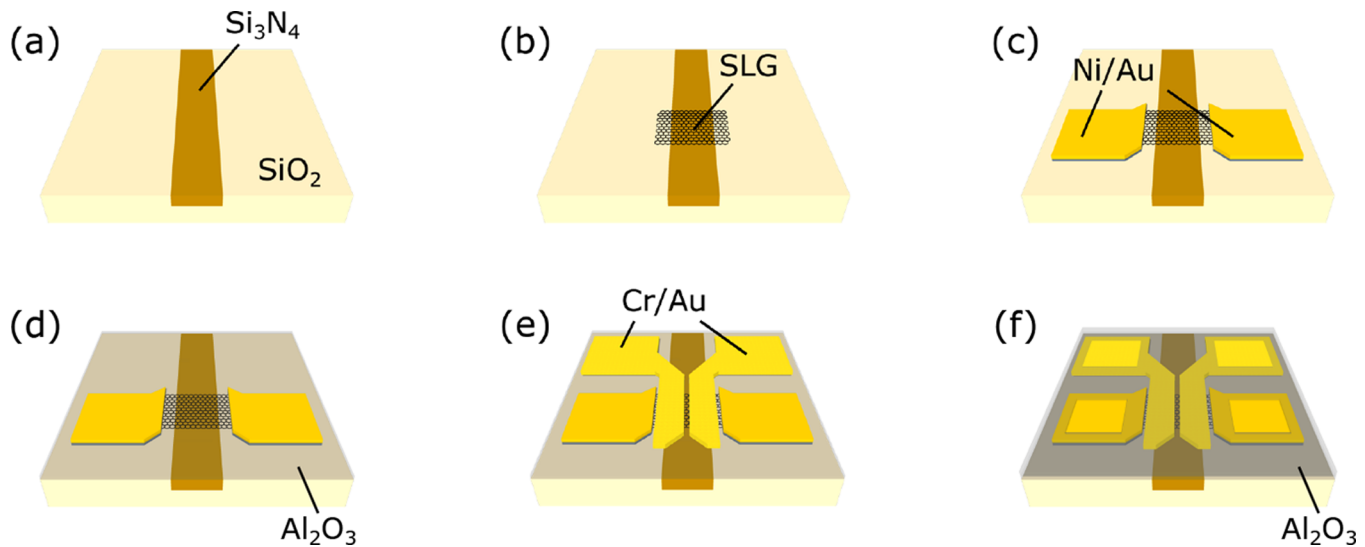


Figure 6. (a) Planarized SiN waveguide. (b) SLG transfer and shaping by oxygen plasma etch. (c) Ni/Au contacts to SLG channel. (d) Al_2O_3 gate oxide deposition. (e) Cr/Au evaporation of split-gate structure. (f) Al_2O_3 encapsulation and contact pads opening.

lead crossing the waveguide behind the active region of the devices (Figure 4b), we measure both GPDs individually, as well as combined. Figure 4c is a false color SEM of the active region of both detectors. Since each GPD is designed to maximally absorb over the length of the device, the power rapidly decays along the propagation direction after the first GPD. We thus place the second device $\sim 1 \mu\text{m}$ from the first.

Figure 4d,e plots the photovoltage maps for both GPDs at $P_{\text{in}} \sim 70 \mu\text{W}$. The GPD closer to the input GC (A) absorbs most of the light and has the 6-fold pattern typical of PTE (Figure 4d). The photoresponse of the second GPD (B) is weaker, due to light absorption in SLG and metal. A 6-fold pattern is not observed, due to the photocurrents being generated in the junctions between gated and ungated sections at either end of the SLG channel. Figure 4f,g shows photovoltage maps of the combination of both GPDs. The response in series is in Figure 4f, while the sum is in Figure 4g. The two plots are in good agreement, confirming that $V_{\text{ph,A+B}} = V_{\text{ph,A}} + V_{\text{ph,B}}$. In order to increase R_V in long (tens of μm) PTE-GPDs with absorption only in the SLG channel, one could therefore add the voltages generated in different sections by subdividing the channel into several shorter devices and connecting them as cascaded GPDs. To minimize the metal leads for contacting and connecting individual devices, this configuration could comprise individually gated devices with alternating p–n junctions to form a meandered structure. This would ideally be implemented with transparent gates, such as indium tin oxide, or a second SLG, at a distance far enough from the channel, to avoid additional losses. In principle, there is no limit to downscaling individual devices along the waveguide. However, as this would increase R by reducing the width of the SLG channels between drain and source (all the more in a series connection) and therefore harm speed and noise performance, downscaling to submicron segments can become impractical in connected configurations.

To evaluate the frequency response, we use the optical heterodyne setup in Figure 5a, combing optical signals at different frequencies. The channel is contacted with an RF probe in G-S configuration. The output of our tunable laser source is combined with a fixed-wavelength laser diode (Thorlabs SFL1550P), and the GPDs' response to the

amplitude beating at the difference frequency is monitored with an electrical spectrum analyzer (ESA, Agilent PSX N9030A). The output signal power of each of the two sources is $\sim 3 \text{ dBm}$. We combine the signals in a 50:50 fiber coupler and, prior to coupling into the SiN waveguide, amplify the combined beating signal up to 15 dBm ($\sim 30 \text{ mW}$) using an erbium-doped fiber amplifier (EDFA, Keyopsys CEFA-C-HG) to increase the output signal detected at the ESA. We monitor the signal stability (i.e., output power and position of the difference frequency) using a reference PD and an oscilloscope. To overcome the signal reduction due to impedance mismatch between the device R and 50Ω of the measurement equipment, we use an additional low noise amplifier (LNA) between GPD and ESA. To calibrate our RF setup prior to measuring the frequency response, we independently record the response of LNA and the remaining measurement setup to a low power (-80 dBm) input from a 50 GHz signal generator.

Figure 5b plots the calibrated response (black squares) to the beating signal at different frequencies, while the split-gate is biased to set an operating point in the p–n junction regime resulting in the largest photoresponse under CW illumination in Figure 3. The response stays within 3 dB of the low-frequency (1 GHz) reference power until 40 GHz, the limit of our measurement setup.

To determine the cutoff, we therefore modify the setup (Figure 5c) to perform impulse response measurements, where the response to ultrashort ($\sim 150 \text{ fs}$) optical pulses is monitored with an oscilloscope. For excitation, we use the idler of an optical parametric oscillator, pumped by a Ti:Sa mode-locked laser at $1.55 \mu\text{m}$, attenuated in free-space prior to coupling into the optical fiber. Figure 5d is the measured impulse response at the same operating point as for the heterodyne measurements. We obtain a pulse duration $\Delta t \sim 11 \text{ ps}$ from the full width at half-maximum (FWHM), assuming a Gaussian pulse shape. For Gaussian-shaped pulses, the time-bandwidth product is ~ 0.44 .¹⁰⁶ From this, we estimate $f_{3\text{dB}} \sim 0.44/\Delta t \sim 40 \text{ GHz}$. The fast Fourier transform of the pulse is in Figure 5b (red circles) after calibration. The trace is in good agreement with the heterodyne response and drops below -3 dB at $\sim 42 \text{ GHz}$. This is consistent with other reports of high-speed MC-SLG-based PTE GPDs, such as the

~ 42 GHz in ref 47, but slower than the highest ~ 65 GHz of ref 45. However, our $f_{3\text{dB}} \sim 42$ GHz is the highest reported to date for PTE-based on-chip GPDs made from CVD SLG.

In summary, we reported waveguide-integrated, plasmonic enhanced GPDs with an external responsivity ~ 12.2 V/W, a -3 dB cutoff ~ 42 GHz, and small ($\sim 3\text{--}20 \mu\text{m}^2$) device footprints, using CVD SLG on SiN. We exploited the integration of an SPP waveguide with an SLG p–n junction to enhance light–SLG interaction and create a confined electron heat-source to obtain a strong, PTE-dominated photoresponse. This paves the way to power-efficient receivers for optoelectronics.

METHODS

Plasmonic Enhanced GPD Fabrication. Figure 6 summarizes the fabrication of our GPDs. Planarized SiN waveguides (Figure 6a, 260 nm high, width 0.8–1.5 μm) on 15 μm SiO₂ are prepared as follows. The SiN layer is first deposited by low-pressure (LP) CVD. The SiN photonic waveguides are then defined by electron beam lithography (EBL) and reactive ion etching. For surface planarization, a 1.6- μm -thick boron–phosphorus tetraethyl orthosilicate (BPTEOS) layer is deposited as top cladding and subsequently etched to a final thickness ~ 20 nm on top of the SiN waveguides, avoiding chemical mechanical polishing. SLG is grown on prepatterned, electropolished Cu with Cr nucleation sites as in ref 89. After an initial annealing in argon (10 min), SLG growth is initiated at 25 mbar with argon, hydrogen, and methane flowing at 900, 100, and 1 standard cubic centimeters per minute (scm), respectively. After growth, SLG single crystals are placed onto the photonic chips by semidry transfer,⁸⁹ comprising the spin-coating of a poly(methyl methacrylate) (PMMA) support layer, the attachment of a Kapton frame for handling, electrochemical delamination of SLG in sodium hydroxide, and the lamination onto the target substrate with the help of a micromanipulator to align the crystals with the photonic structures. After transfer, the PMMA support layer is removed by immersion in acetone and AR600-71 remover. A new PMMA etch mask is then used to shape the device channel and remove excess SLG over GCs and waveguides, defined using EBL. This is followed by oxygen plasma etching at 3 W (Figure 6b). Next, contacts are defined by another EBL step. Metallization (15 nm Ni/40 nm Au) is done by sputtering, thermal evaporation, and lift-off in acetone (Figure 6c). 30 nm Al₂O₃ is used as gate dielectric, via atomic layer deposition (ALD) (Figure 6d). An additional EBL step and electron beam evaporation are used to fabricate the plasmonic split gates (Figure 6e). To encapsulate the device and prevent air breakdown in the gap between gate contacts when ~ 10 V is applied, we deposit another 40 nm Al₂O₃ by ALD. A laser writer defines an etch mask to access contacts (Figure 6f).

The quality of SLG is monitored by Raman spectroscopy at all critical points during the fabrication process, using a Renishaw InVia equipped with a 50 \times objective (numerical aperture NA = 0.75) at 514.5 nm with power below 0.5 mW to exclude heating effects. Representative spectra of SLG on Cu (after removal of Cu background photoluminescence¹⁰⁷), after transfer onto the waveguide, and after complete device fabrication, are shown in Figure 7. The absence of a D peak indicates that negligible defects are introduced during fabrication. The 2D peaks are single-Lorentzian, confirming the presence of SLG.^{108,109} On Cu, the position and FWHM of

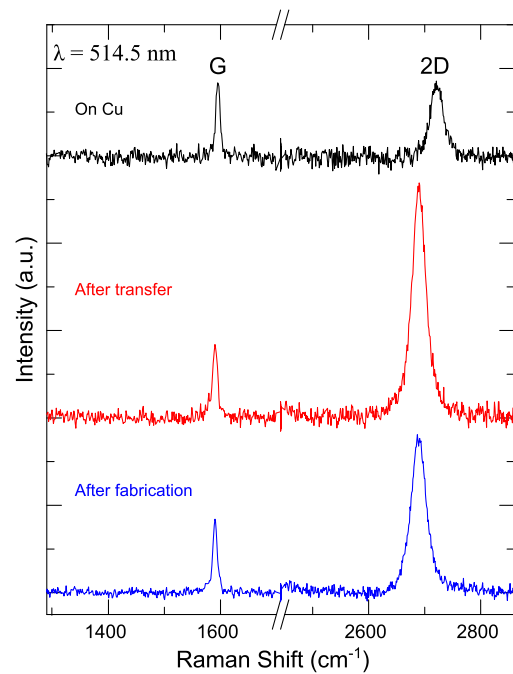


Figure 7. Raman spectra at 514.5 nm for SLG as grown on Cu (black), after transfer onto the SiN waveguide (red), and after device fabrication (blue). All spectra are normalized to the intensity of the G peak, $I(\text{G})$, and are shown after subtraction of the substrate signals.

the G peak are $\text{Pos}(\text{G}) \sim 1595 \text{ cm}^{-1}$ and $\text{FWHM}(\text{G}) \sim 8 \text{ cm}^{-1}$. The position of the 2D peak, $\text{Pos}(2\text{D})$, is $\sim 2721 \text{ cm}^{-1}$ with $\text{FWHM}(2\text{D}) \sim 27 \text{ cm}^{-1}$. The 2D to G peak intensity, $I(2\text{D})/I(\text{G})$, and area, $A(2\text{D})/A(\text{G})$, ratios are ~ 1 and ~ 3.2 . After transfer, $\text{Pos}(\text{G}) \sim 1590 \text{ cm}^{-1}$, $\text{FWHM}(\text{G}) \sim 10 \text{ cm}^{-1}$, $\text{Pos}(2\text{D}) \sim 2690 \text{ cm}^{-1}$, $\text{FWHM}(2\text{D}) \sim 28 \text{ cm}^{-1}$, $I(2\text{D})/I(\text{G}) \sim 3.2$, and $A(2\text{D})/A(\text{G}) \sim 8.6$. This corresponds to ~ 250 meV doping^{110,111} and a carrier concentration $\sim 4 \times 10^{12} \text{ cm}^{-2}$. After final encapsulation, $\text{Pos}(\text{G}) \sim 1590 \text{ cm}^{-1}$, $\text{FWHM}(\text{G}) \sim 9 \text{ cm}^{-1}$, $\text{Pos}(2\text{D}) \sim 2689 \text{ cm}^{-1}$, $\text{FWHM}(2\text{D}) \sim 30 \text{ cm}^{-1}$, $I(2\text{D})/I(\text{G}) \sim 2.2$, $A(2\text{D})/A(\text{G}) \sim 7.6$, indicating a residual ~ 350 meV ($n \sim 7 \times 10^{12} \text{ cm}^{-2}$) doping. This additional doping only affects the CNP position and the gate-voltage needed to generate the p–n junctions, since the split-gate structure sets the doping during device operation.

Modeling and Simulations. Plasmonic gap width, SLG placement, and thickness of metal and oxide structures are the key parameters to be optimized to achieve maximum photovoltage. To do so, we build a device model in the layout environment of a commercial eigenmode solver (Lumerical MODE Solutions). In order to model SLG in the optical solver and subsequent calculations consistently, we use a volumetric permittivity material model, in which SLG is described as cuboid with finite thickness $t = 0.34 \text{ nm}$, and in-plane (ϵ_{\parallel}) and out-of plane (ϵ_{\perp}) permittivity are defined as independent tensor elements. To calculate the in-plane relative permittivity for SLG, we use¹¹²

$$\epsilon(\omega) = \epsilon'(\omega) + i\epsilon''(\omega) = \epsilon_r + \frac{i\sigma(\omega)}{\epsilon_0\omega t} \quad (4)$$

where $\epsilon'(\omega)$ and $\epsilon''(\omega)$ are the real and imaginary part of the relative permittivity $\epsilon(\omega)$, $\sigma(\omega)$ is the SLG optical conductivity, ω is the angular frequency, ϵ_r is the background relative permittivity (whose frequency-dependence is ignored

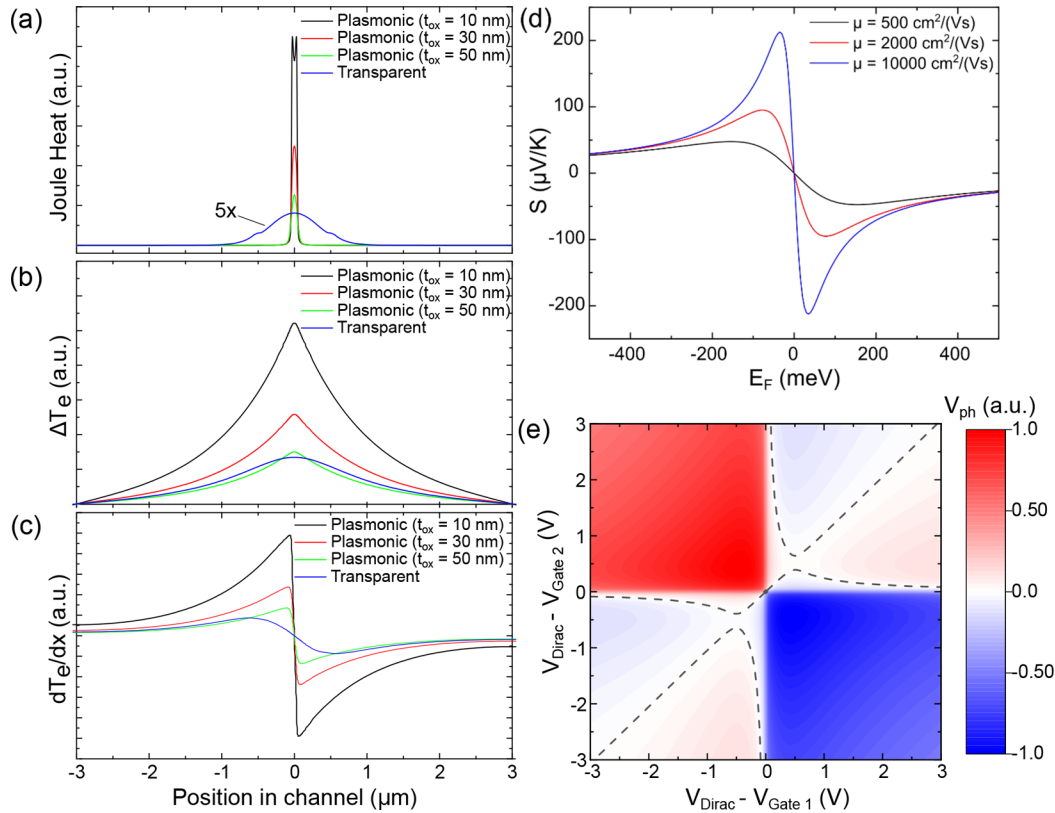


Figure 8. (a) Joule heat source, (b) T_e profile, (c) $\frac{dT_e}{dx}$ across the SLG channel (x -direction) for a representative GPD with plasmonic gates at different heights above the channel compared to gates transparent at $1.55 \mu\text{m}$. The zero position marks the center of the channel between the source and drain contact. (d) Calculated dependence of S on E_F for different μ and constant minimum conductivity. (e) Simulated photovoltage map. $V_{Dirac} - V_{Gate}$ shows the gating relative to the CNP. The dotted line indicates the zero photovoltage line.

in the small $1.5\text{--}1.6 \mu\text{m}$ range under consideration), and ϵ_0 is the free-space permittivity. $\sigma(\omega)$ is obtained by linear response¹¹³ in the random-phase approximation,¹¹² and contains terms describing intraband and interband transitions. While the former can be evaluated analytically,¹¹³ the interband term requires a numerical solution.^{112,113} The out-of-plane component of the dielectric tensor matches ϵ_r .

We then run the eigenmode solver, using the relative permittivity function for SLG, and select the fundamental (gap plasmon) mode (typical propagation losses >5000 dB/cm) for further processing. We export the simulation mesh grid positions, electric \mathbf{E} and magnetic \mathbf{H} data, effective refractive index ($n_{\text{eff}} = \beta/k_0$, where β is the propagation constant of the mode and k_0 is the free space wavevector¹¹⁴), and all relevant geometric parameters such as w_{gap} , t_{ox} , and gate width.

A crucial intermediate step requires the determination of the $T_e(x)$ profile in the SLG channel. The first step establishes the operating regime. As discussed in refs 115 and 116, the energy delivered to the electronic carrier distribution by pumping SLG with a pulsed laser can be sufficiently high to result in $T_e(x) > 1000$ K. When modeling photoexcited SLG under these conditions, one has to take into account the $T_e(x)$ dependence^{115,116} of all thermodynamic and transport parameters in eqs 1–3, i.e., μ_c , $\sigma(x)$, $\kappa_c(x)$, resulting in a nonlinear system of coupled equations.

The contrasting case, “weak heating”, is characterized by $|\Delta T_e(x)| \ll T_1$.^{64,83} Under this condition, eqs 1–3 can be solved to linear order in the local $T_e(x)$ fluctuation, evaluating all thermodynamic and transport parameters at $T_e(x) = T_1$. A

single μ_c is established, following photoexcitation, by electron–electron interactions across valence and conduction bands, and the thermal conductivity, calculated from the Wiedemann–Franz law $\kappa_e = \pi^2 k_B^2 T_e \sigma / (3e^2)$,⁷⁶ is uniform.

The intended operation of our GPD is under CW or, during data reception, quasi-CW (i.e., the pulse duration exceeds the cooling time of the hot-carrier distribution) illumination with low $P_{\text{in}} < 0.1$ mW at in-plane incidence. Furthermore, a linear dependence of V_{ph} on P_{in} , such as in Figure 3d, is observed.⁶⁴ Thus, our device operates in the “weak heating” regime.

In order to evaluate eq 3, we need to specify the cooling length ξ and the light absorption heat source. In principle, ξ , which describes the energy transfer from the electronic system to the optical phonons,⁶⁷ depends on $T_e(x)$ and n . However, in “weak heating”, the $T_e(x)$ dependence can be neglected, and n is uniform in the device (with opposite sign in the two regions of the p–n junction) when the photoresponse is maximal. For these reasons, in our calculations, we assume a constant $\xi = 1 \mu\text{m}$, consistent with experimental values.^{47,80} $J(x)$ is calculated from the simulated electric field as the time average of the electric power dissipation density:^{102,103}

$$J(x) = \frac{1}{2} \omega \epsilon'' |\mathbf{E}|^2 = \frac{1}{2} \frac{\sigma}{t} \mathbf{E} \cdot \mathbf{E}^* \quad (5)$$

To relate $J(x)$ to physically meaningful quantities, we integrate the normal component of the time-averaged Poynting vector over the simulation region and normalize it to a given input power.

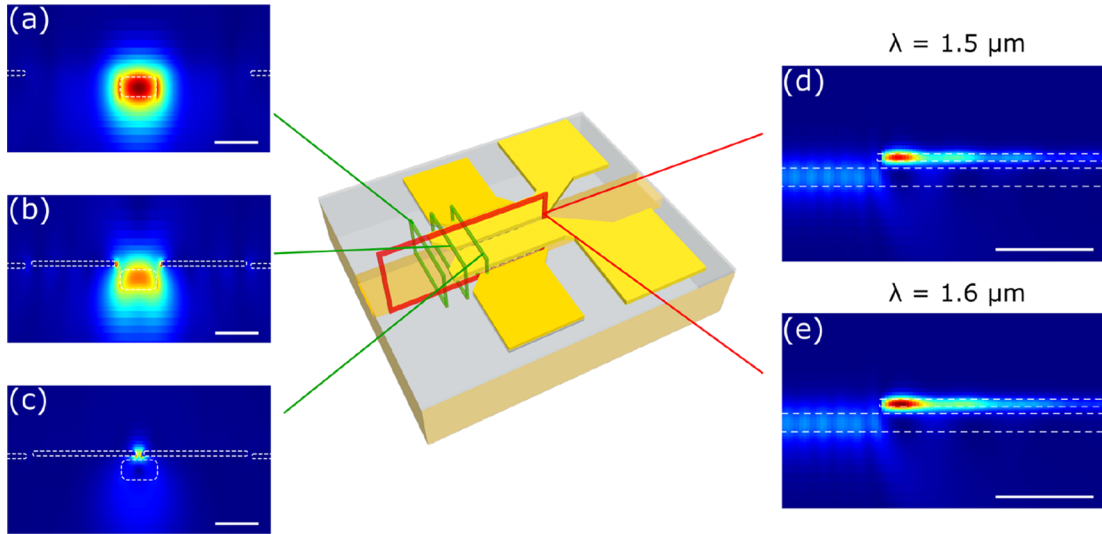


Figure 9. Field distribution (a) before GPD, (b) during transition, and (c) at the start of the split-gate/SPP waveguide. Scale bar: 1 μm . (d,e) $|E|^2$ along the center (red box) of dielectric waveguide and GPD at (d) 1.5 μm and (e) 1.6 μm . Scale bar: 3 μm .

After solving eq 3 for the $T_e(x)$ fluctuation profile, $\Delta T_e(x)$, we take its derivative with respect to x and obtain the second factor of the integrand in eq 1. Figure 8a–c compares the absorption heat source, the resulting $T_e(x)$ profile, and its derivative for a representative GPD in the presence of a plasmonic split-gate at different heights over the SLG channel, to an unperturbed fundamental dielectric waveguide mode, where the p–n junction is generated by a transparent (at the chosen λ) gate, such as a split-gate made from a second SLG at a separation large enough to avoid additional optical losses. The beneficial role of plasmonic enhancement, with all other parameters fixed, for a sharper increase in $T_e(x)$ translates to larger V_{ph} if SLG is close to the SPP waveguide (<50 nm).

To model S along the channel, we use a Drude conductivity expression,¹⁰⁴ simplified to $\sigma = \sigma_{\text{min}} + ne\mu$, and $E_{\text{F}} = \pm \hbar v_{\text{F}} \sqrt{n\pi}$, where \hbar is the reduced Planck constant and v_{F} is the Fermi velocity, as discussed in ref 55, in eq 2. This yields

$$S(\mu, \mu_c) = \frac{2\pi k_{\text{B}}^2 T_{\text{d}} \mu_c}{3\hbar^2 v_{\text{F}}^2} \times \frac{\mu}{\sigma_{\text{min}} + \frac{\mu_c^2 e}{\pi \hbar^2 v_{\text{F}}^2} \times \mu} \quad (6)$$

To stress the dependence of S on μ and σ_{min} (see Figure 8d), this can be written as

$$S(\mu) = C_1 \times \frac{\mu}{\sigma_{\text{min}} + C_2 \times \mu} \quad (7)$$

where $C_1 = \frac{2\pi k_{\text{B}}^2 T_{\text{d}} \mu_c}{3\hbar^2 v_{\text{F}}^2}$ and $C_2 = \frac{\mu_c^2 e}{\pi \hbar^2 v_{\text{F}}^2}$

We then assume that the structure is gated to achieve the maximum S below the gates, as for eq 2 (opposite in sign but equal in magnitude for the p–n case) and approximate the gap with a linear interpolation between the two. Combining both factors in eq 1 and computing the integral yields V_{ph} or R_{V} (if divided by P_{in}) as a figure of merit to assess different designs:

$$R_{\text{V}} = \frac{|V_{\text{ph}}|}{P_{\text{in}}} = \frac{1}{P_{\text{in}}} \left| \int S(x) \frac{dT_e(x)}{dx} dx \right| \quad (8)$$

To calculate R_{V} or photovoltage maps as in Figure 8e, we first generate the S profile for all voltage combinations and then proceed via eq 8 or 1.

We then perform a sweep of gap width, SLG position, gate oxide thickness, and gate contact height as a function of μ in SLG and ϵ_r . As for Figure 8, shorter distances between SLG channel and SPP waveguide yield larger signals. Furthermore, the SPP waveguide width affects the expected photovoltage in two ways: (1) Narrower confinement improves the field strength at the SLG channel and R_{V} at the cost of higher propagation losses; (2) the ungated SLG at the center of the device without maximum S shrinks with smaller gaps. The device parameters are then chosen based on these trends, taking into account fabrication complexity, robustness to processing-induced deviations (e.g., suppression of fundamental gap plasmon mode below a certain gap width), reliability (e.g., oxide breakdown), and outcomes of FDTD simulations on coupling and propagation.

Extracting \mathbf{E} and \mathbf{H} of the fundamental mode in the hybrid region is sufficient for the design of the device cross section. However, it does not capture the field distribution along the device, since optical losses, transition from dielectric to plasmonic waveguide, and power exchange between different modes that coexist in the hybrid region remain unaccounted for. We thus perform finite-difference time domain (FDTD) simulations in Lumerical FDTD. We construct a device model in the same way as for the eigenmode analysis and adjust the source settings to 1.5–1.6 μm . We launch the fundamental quasi-TE mode of the SiN waveguide toward the GPD and use frequency domain field monitors with various orientations (parallel and perpendicular to the propagation direction) to track the field and power profiles at different points.

Taper-assisted butt-coupling (end-to-end alignment) is a good option to achieve low (<0.6 dB)¹¹⁷ insertion loss (IL) for the transition from optical to plasmonic modes. However, since evanescent coupling (lateral or vertical alignment) provides simpler fabrication¹¹⁸ and greater flexibility for the placement of devices on top of integrated optical circuits,¹¹⁹ we use this here despite higher IL. The coexistence of the plasmonic and dielectric waveguide leads to oscillating power exchange between both structures.^{118–120} For the highest

coupling efficiency, the vertical distance between these waveguides is typically >150 nm,^{118,119} exploiting the interference between quasi-even and quasi-odd eigenmodes.^{118–120} In our design, we keep this separation small (tens of nm) to ensure overlap between SLG and gap plasmon mode, to avoid a long (>5 μm) coupling length,¹¹⁸ and to create a sharper concentration of power close to the front of the plasmonic structure. Within these constraints, the simulated coupling efficiency for this transition is ~ 20 – 40% , depending on w_{gap} , t_{ox} , t_{gate} , as defined in Figure 1, and the dimensions of the underlying SiN waveguide. Figure 9a–c plots the field at three cross sections of a representative GPD. We see transitions from the injected mode in the dielectric waveguide to a field distribution resembling the fundamental gap plasmon.

To obtain the largest R_V , the electric field distribution along the propagation directions needs to be considered. Light absorption in SLG or in the plasmonic structure along the device leads to an exponential decay of optical power.⁶² To optimize R_V , a compact (<10 μm) device with optimized peak absorption and minimal drop-off is preferable. Figure 9d,e displays the electric field intensity from a vertical field monitor along the center line of the GPD, at two wavelengths. As expected for this nonadiabatic transition with fast decrease (<1 μm) of the taper cross section down to the target gap size, scattering and reflections at the start of the hybrid region reduce the power at the GPD, but the desired sharp intensity profile over length scales that match the fabricated SLG channel widths is achieved. Consequently, we place the SLG channel 100 nm after the SPP structure has reached its final gap width. The comparison of field intensities for 1.5 and 1.6 μm on the same color scale in Figure 9d,e reveals a larger peak intensity and a longer interaction length for the latter, which indicates improved coupling efficiency at larger λ , as for the wavelength-dependent R_V in Figure 3c.

AUTHOR INFORMATION

Corresponding Author

*E-mail: acf26@eng.cam.ac.uk.

ORCID

Jakob E. Muench: 0000-0002-3124-3385

Marco A. Giambra: 0000-0002-1566-2395

Camilla Coletti: 0000-0002-8134-7633

Andrea C. Ferrari: 0000-0003-0907-9993

Notes

The authors declare no competing financial interest.

ACKNOWLEDGMENTS

We acknowledge funding from EU Graphene Flagship, ERC Grant Hetero2D, EPSRC Grants EP/K01711X/1, EP/K017144/1, EP/N010345/1, EP/L016087/1, and DSTL.

REFERENCES

- (1) Cisco Visual Networking Index: Forecast and Methodology (2016–2021); Cisco, 2017. <https://www.cisco.com/c/en/us/solutions/collateral/service-provider/visual-networking-index-vni/complete-white-paper-c11-481360.pdf>.
- (2) Andrews, J. G.; Buzzi, S.; Choi, W.; Hanly, S. V.; Lozano, A.; Soong, A. C. K.; Zhang, J. C. *IEEE J. Sel. Areas Commun.* **2014**, *32*, 1065–1082.
- (3) Osseiran, A.; Boccardi, F.; Braun, V.; Kusume, K.; Marsch, P.; Maternia, M.; Queseth, O.; Schellmann, M.; Schotten, H.; Taoka, H.; et al. *IEEE Commun. Mag.* **2014**, *52*, 26–35.
- (4) Glick, M.; Kimmerling, L. C.; Pfahl, R. C. *Opt. Photonics News* **2018**, *29*, 36–41.
- (5) Sparks, P. *Route to a trillion devices - The outlook for IoT investment to 2035*; ARM, 2017.
- (6) Rumley, S.; Nikolova, D.; Hendry, R.; Li, Q.; Calhoun, D.; Bergman, K. J. *J. Lightwave Technol.* **2015**, *33*, 547–562.
- (7) Cheng, Q.; Bahadori, M.; Glick, M.; Rumley, S.; Bergman, K. *Optica* **2018**, *5*, 1354–1370.
- (8) Thomson, D.; Zilkie, A.; Bowers, J. E.; Komljenovic, T.; Reed, G. T.; Vivien, L.; Marris-Morini, D.; Cassan, E.; Virost, L.; Fédéli, J. J. *Opt.* **2016**, *18*, 073003.
- (9) Absil, P. P.; Verheyen, P.; De Heyn, P.; Pantouvaki, M.; Lepage, G.; De Coster, J.; Van Campenhout, J. *Opt. Express* **2015**, *23*, 9369–9378.
- (10) Atabaki, A. H.; Moazeni, S.; Pavanello, F.; Gevorgyan, H.; Notaros, J.; Alloatti, L.; Wade, M. T.; Sun, C.; Kruger, S. A.; Meng, H.; et al. *Nature* **2018**, *556*, 349–354.
- (11) Subbaraman, H.; Xu, X.; Hosseini, A.; Zhang, X.; Zhang, Y.; Kwong, D.; Chen, R. T. *Opt. Express* **2015**, *23*, 2487–2511.
- (12) Wooten, E. L.; Kissa, K. M.; Yi-Yan, A.; Murphy, E. J.; Lafaw, D. A.; Hallemeier, P. F.; Maack, D.; Attanasio, D. V.; Fritz, D. J.; McBrien, G. J.; et al. *IEEE J. Sel. Top. Quantum Electron.* **2000**, *6*, 69–82.
- (13) Wang, C.; Zhang, M.; Chen, X.; Bertrand, M.; Shams-Ansari, A.; Chandrasekhar, S.; Winzer, P.; Lončar, M. *Nature* **2018**, *562*, 101–104.
- (14) Nagarajan, R.; Kato, M.; Pleumeekers, J.; Evans, P.; Corzine, S.; Hurtt, S.; Dentai, A.; Murthy, S.; Missey, M.; Muthiah, R.; et al. *IEEE J. Sel. Top. Quantum Electron.* **2010**, *16*, 1113–1125.
- (15) Hosseini, A.; Lu, M.; Going, R.; Samra, P.; Amiralzadeh, S.; Nguyen, A.; Rahn, J.; Dominic, V.; Awadalla, A.; Corzine, S.; et al. *Opt. Express* **2017**, *25*, 18853–18862.
- (16) Michel, J.; Liu, J.; Kimerling, L. C. *Nat. Photonics* **2010**, *4*, 527–534.
- (17) Hawkins, A. R.; Wu, W.; Abraham, P.; Streubel, K.; Bowers, J. E. *Appl. Phys. Lett.* **1997**, *70*, 303–305.
- (18) Chang, H.; Kuo, Y.; Jones, R.; Barkai, A.; Bowers, J. E. *Opt. Express* **2010**, *18*, 23891–23899.
- (19) Chrostowski, L.; Hochberg, M. *Silicon Photonics Design: From Devices to Systems*; Cambridge University Press: Glasgow, 2015.
- (20) Vivien, L.; Osmond, J.; Fédéli, J.; Marris-Morini, D.; Crozat, P.; Damlencourt, J.; Cassan, E.; Lecunff, Y.; Laval, S. *Opt. Express* **2009**, *17*, 6252–6257.
- (21) DeRose, C. T.; Trotter, D. C.; Zortman, W. A.; Starbuck, A. L.; Fisher, M.; Watts, M. R.; Davids, P. S. *Opt. Express* **2011**, *19*, 24897–24904.
- (22) Vivien, L.; Polzer, A.; Marris-Morini, D.; Osmond, J.; Hartmann, J. M.; Crozat, P.; Cassan, E.; Kopp, C.; Zimmermann, H.; Fédéli, J. M. *Opt. Express* **2012**, *20*, 1096–1101.
- (23) Novack, A.; Gould, M.; Yang, Y.; Xuan, Z.; Streshinsky, M.; Liu, Y.; Capellini, G.; Lim, A. E.; Lo, G.; Baehr-Jones, T.; et al. *Opt. Express* **2013**, *21*, 28387–28393.
- (24) Chen, H.; Verheyen, P.; De Heyn, P.; Lepage, G.; De Coster, J.; Balakrishnan, S.; Yao, W.; Shen, L.; Roelkens, G.; Van Campenhout, J. *Opt. Express* **2016**, *24*, 4622–4631.
- (25) Salamin, Y.; Ma, P.; Baeuerle, B.; Emboras, A.; Fedoryshyn, Y.; Heni, W.; Cheng, B.; Josten, A.; Leuthold, J. *ACS Photonics* **2018**, *5*, 3291–3297.
- (26) Wang, J.; Lee, S. *Sensors* **2011**, *11*, 696–718.
- (27) Ye, H.; Yu, J. *Sci. Technol. Adv. Mater.* **2014**, *15*, 024601.
- (28) Sorianello, V.; De Iacovo, A.; Colace, L.; Fabbri, A.; Tortora, L.; Buffagni, E.; Assanto, G. *Appl. Phys. Lett.* **2012**, *101*, 081101.
- (29) Liu, J.; Cannon, D. D.; Wada, K.; Ishikawa, Y.; Jongthammanurak, S.; Danielson, D. T.; Michel, J.; Kimerling, L. C. *Appl. Phys. Lett.* **2005**, *87*, 011110.
- (30) Rahim, A.; Ryckeboer, E.; Subramanian, A. Z.; Clemmen, S.; Kuyken, B.; Dhakal, A.; Raza, A.; Hermans, A.; Muneeb, M.; Dhoore, S.; et al. *J. Lightwave Technol.* **2017**, *35*, 639–649.

- (31) Romagnoli, M.; Sorianoello, V.; Midrio, M.; Koppens, F. H. L.; Huyghebaert, C.; Neumaier, D.; Galli, P.; Templ, W.; D'Errico, A.; Ferrari, A. C. *Nat. Rev. Mater.* **2018**, *3*, 392–414.
- (32) Liu, M.; Yin, X.; Ulin-Avila, E.; Geng, B.; Zentgraf, T.; Ju, L.; Wang, F.; Zhang, X. *Nature* **2011**, *474*, 64–67.
- (33) Liu, M.; Yin, X.; Zhang, X. *Nano Lett.* **2012**, *12*, 1482–1485.
- (34) Hu, Y.; Pantouvaki, M.; Van Campenhout, J.; Brems, S.; Asselberghs, I.; Huyghebaert, C.; Absil, P.; Van Thourhout, D. *Laser Photon. Rev.* **2016**, *10*, 307–316.
- (35) Phare, C. T.; Daniel Lee, Y.; Cardenas, J.; Lipson, M. *Nat. Photonics* **2015**, *9*, 511–514.
- (36) Sorianoello, V.; Midrio, M.; Romagnoli, M. *Opt. Express* **2015**, *23*, 6478–6490.
- (37) Sorianoello, V.; Midrio, M.; Contestabile, G.; Asselberghs, I.; Van Campenhout, J.; Huyghebaert, C.; Goykhman, I.; Ott, A. K.; Ferrari, A. C.; Romagnoli, M. *Nat. Photonics* **2018**, *12*, 40–44.
- (38) Giambra, M. A.; Sorianoello, V.; Miseikis, V.; Marconi, S.; Montanaro, A.; Galli, P.; Pezzini, S.; Coletti, C.; Romagnoli, M. *Opt. Express* **2019**, *27*, 20145–20155.
- (39) Sun, Z.; Martinez, A.; Wang, F. *Nat. Photonics* **2016**, *10*, 227–238.
- (40) Gan, X.; Shiue, R.; Gao, Y.; Meric, I.; Heinz, T. F.; Shepard, K.; Hone, J.; Assefa, S.; Englund, D. *Nat. Photonics* **2013**, *7*, 883–887.
- (41) Pospischil, A.; Humer, M.; Furchi, M. M.; Bachmann, D.; Guider, R.; Fromherz, T.; Mueller, T. *Nat. Photonics* **2013**, *7*, 892–896.
- (42) Wang, X.; Cheng, Z.; Xu, K.; Tsang, H. K.; Xu, J. *Nat. Photonics* **2013**, *7*, 888–891.
- (43) Goykhman, I.; Sassi, U.; Desiatov, B.; Mazurski, N.; Milana, S.; De Fazio, D.; Eiden, A.; Khurgin, J.; Shappir, J.; Levy, U.; et al. *Nano Lett.* **2016**, *16*, 3005–3013.
- (44) Schall, D.; Neumaier, D.; Mohsin, M.; Chmielak, B.; Bolten, J.; Porschatis, C.; Prinzen, A.; Matheisen, C.; Kuebart, W.; Junginger, B.; et al. *ACS Photonics* **2014**, *1*, 781–784.
- (45) Schuler, S.; Schall, D.; Neumaier, D.; Dobusch, L.; Bethge, O.; Schwarz, B.; Krall, M.; Mueller, T. *Nano Lett.* **2016**, *16*, 7107–7112.
- (46) Schuler, S.; Schall, D.; Neumaier, D.; Schwarz, B.; Watanabe, K.; Taniguchi, T.; Mueller, T. *ACS Photonics* **2018**, *5*, 4758–4763.
- (47) Shiue, R. J.; Gao, Y.; Wang, Y.; Peng, C.; Robertson, A. D.; Efetov, D. K.; Assefa, S.; Koppens, F. H. L.; Hone, J.; Englund, D. *Nano Lett.* **2015**, *15*, 7288–7293.
- (48) Schall, D.; Porschatis, C.; Otto, M.; Neumaier, D. *J. Phys. D: Appl. Phys.* **2017**, *50*, 124004.
- (49) Schall, D.; Pallecchi, E.; Ducournau, G.; Avramovic, V.; Otto, M.; Neumaier, D. *Optical Fiber Communication Conference, M2I.4*; Optical Society of America, 2018.
- (50) Ding, Y.; Cheng, Z.; Zhu, X.; Yvind, K.; Dong, J.; Galili, M.; Hu, H.; Mortensen, N. A.; Xiao, S.; Oxenlowe, L. K. **2018**, arXiv:1808.04815. ArXiv e-Print archive. <https://arxiv.org/abs/1808.04815>.
- (51) Ma, P.; Salamin, Y.; Baeuerle, B.; Josten, A.; Heni, W.; Emboras, A.; Leuthold, J. *ACS Photonics* **2019**, *6*, 154–161.
- (52) Ma, Z.; Kikunage, K.; Wang, H.; Sun, S.; Amin, R.; Tahersima, M.; Maiti, R.; Miscuglio, M.; Dalir, H.; Sorger, V. J. **2018**, arXiv:1812.00894. ArXiv e-Print archive. <https://arxiv.org/abs/1812.00894>.
- (53) Wang, J.; Cheng, Z.; Chen, Z.; Wan, X.; Zhu, B.; Tsang, H. K.; Shu, C.; Xu, J. *Nanoscale* **2016**, *8*, 13206–13211.
- (54) Gao, Y.; Zhou, G.; Zhao, N.; Tsang, H. K.; Shu, C. *Opt. Lett.* **2018**, *43*, 1399–1402.
- (55) Bonaccorso, F.; Sun, Z.; Hasan, T.; Ferrari, A. C. *Nat. Photonics* **2010**, *4*, 611–622.
- (56) Urich, A.; Unterrainer, K.; Mueller, T. *Nano Lett.* **2011**, *11*, 2804–2808.
- (57) Xia, F.; Mueller, T.; Lin, Y.; Valdes-Garcia, A.; Avouris, P. *Nat. Nanotechnol.* **2009**, *4*, 839–843.
- (58) Nair, R. R.; Blake, P.; Grigorenko, A. N.; Novoselov, K. S.; Booth, T. J.; Stauber, T.; Peres, N. M. R.; Geim, A. K. *Science* **2008**, *320*, 1308.
- (59) Dawlaty, J. M.; Shivaraman, S.; Strait, J.; George, P.; Chandrashekhara, M.; Rana, F.; Spencer, M. G.; Veksler, D.; Chen, Y. *Appl. Phys. Lett.* **2008**, *93*, 131905.
- (60) Koppens, F. H.; Mueller, T.; Avouris, P.; Ferrari, A. C.; Vitiello, M. S.; Polini, M. *Nat. Nanotechnol.* **2014**, *9*, 780–793.
- (61) Goossens, S.; Navickaite, G.; Monasterio, C.; Gupta, S.; Piqueras, J. J.; Pérez, R.; Burwell, G.; Nikitskiy, I.; Lasanta, T.; Galán, T.; et al. *Nat. Photonics* **2017**, *11*, 366–371.
- (62) Youngblood, N.; Li, M. *Nanophotonics* **2017**, *6*, 1205–1218.
- (63) Liu, M.; Zhang, X. *Nat. Photonics* **2013**, *7*, 851–852.
- (64) Tielrooij, K.; Piatkowski, L.; Massicotte, M.; Woessner, A.; Ma, Q.; Lee, Y.; Myhro, K. S.; Lau, C. N.; Jarillo-Herrero, P.; van Hulst, N. F.; et al. *Nat. Nanotechnol.* **2015**, *10*, 437–443.
- (65) Mueller, T.; Xia, F.; Avouris, P. *Nat. Photonics* **2010**, *4*, 297–301.
- (66) Echtermeyer, T. J.; Nene, P. S.; Trushin, M.; Gorbachev, R. V.; Eiden, A. L.; Milana, S.; Sun, Z.; Schliemann, J.; Lidorikis, E.; Novoselov, K. S.; et al. *Nano Lett.* **2014**, *14*, 3733–3742.
- (67) Song, J. C. W.; Rudner, M. S.; Marcus, C. M.; Levitov, L. S. *Nano Lett.* **2011**, *11*, 4688–4692.
- (68) Gabor, N. M.; Song, J. C.; Ma, Q.; Nair, N. L.; Taychatanapat, T.; Watanabe, K.; Taniguchi, T.; Levitov, L. S.; Jarillo-Herrero, P. *Science* **2011**, *334*, 648–652.
- (69) Konstantatos, G.; Badioli, M.; Gaudreau, L.; Osmond, J.; Bernechea, M.; de Arquer, F. P. G.; Gatti, F.; Koppens, F. H. L. *Nat. Nanotechnol.* **2012**, *7*, 363–368.
- (70) Vicarelli, L.; Vitiello, M. S.; Coquillat, D.; Lombardo, A.; Ferrari, A. C.; Knap, W.; Polini, M.; Pellegrini, V.; Tredicucci, A. *Nat. Mater.* **2012**, *11*, 865–871.
- (71) Freitag, M.; Low, T.; Xia, F.; Avouris, P. *Nat. Photonics* **2013**, *7*, 53–59.
- (72) Sassi, U.; Parret, R.; Nanot, S.; Bruna, M.; Borini, S.; De Fazio, D.; Zhao, Z.; Lidorikis, E.; Koppens, F. H. L.; Ferrari, A. C.; et al. *Nat. Commun.* **2017**, *8*, 14311.
- (73) Huo, N.; Konstantatos, G. *Adv. Mater.* **2018**, *30*, 1801164.
- (74) Brida, D.; Tomadin, A.; Manzoni, C.; Kim, Y. J.; Lombardo, A.; Milana, S.; Nair, R. R.; Novoselov, K. S.; Ferrari, A. C.; Cerullo, G.; et al. *Nat. Commun.* **2013**, *4*, 1987.
- (75) Tomadin, A.; Brida, D.; Cerullo, G.; Ferrari, A. C.; Polini, M. *Phys. Rev. B* **2013**, *88*, 035430.
- (76) Kittel, C. *Introduction to solid state physics*; Wiley: New York, 1996.
- (77) Bonini, N.; Lazzeri, M.; Marzari, N.; Mauri, F. *Phys. Rev. Lett.* **2007**, *99*, 176802.
- (78) Lazzeri, M.; Piscanec, S.; Mauri, F.; Ferrari, A.; Robertson, J. *Phys. Rev. Lett.* **2005**, *95*, 236802.
- (79) Ashcroft, N.; Mermin, N. *Solid State Physics*; Harcourt College Publishers: Fort Worth, 1976.
- (80) Ma, Q.; Gabor, N. M.; Andersen, T. I.; Nair, N. L.; Watanabe, K.; Taniguchi, T.; Jarillo-Herrero, P. *Phys. Rev. Lett.* **2014**, *112*, 247401.
- (81) Freitag, M.; Low, T.; Avouris, P. *Nano Lett.* **2013**, *13*, 1644–1648.
- (82) Herring, P. K.; Hsu, A. L.; Gabor, N. M.; Shin, Y. C.; Kong, J.; Palacios, T.; Jarillo-Herrero, P. *Nano Lett.* **2014**, *14*, 901–907.
- (83) Castilla, S.; Terrés, B.; Autore, M.; Viti, L.; Li, J.; Nikitin, A. Y.; Vangelidis, I.; Watanabe, K.; Taniguchi, T.; Lidorikis, E.; et al. *Nano Lett.* **2019**, *19*, 2765–2773.
- (84) Novoselov, K. S.; Jiang, D.; Schedin, F.; Booth, T. J.; Khotkevich, V. V.; Morozov, S. V.; Geim, A. K. *Proc. Natl. Acad. Sci. U. S. A.* **2005**, *102*, 10451–10453.
- (85) Fang, Y.; Armin, A.; Meredith, P.; Huang, J. *Nat. Photonics* **2019**, *13*, 1–4.
- (86) Wang, L.; Meric, I.; Huang, P. Y.; Gao, Q.; Gao, Y.; Tran, H.; Taniguchi, T.; Watanabe, K.; Campos, L. M.; Muller, D. A.; et al. *Science* **2013**, *342*, 614–617.
- (87) Purdie, D. G.; Pugno, N. M.; Taniguchi, T.; Watanabe, K.; Ferrari, A. C.; Lombardo, A. *Nat. Commun.* **2018**, *9*, 5387.

- (88) De Fazio, D.; Purdie, D. G.; Ott, A. K.; Braeuninger-Weimer, P.; Khodkov, T.; Goossens, S.; Taniguchi, T.; Watanabe, K.; Livreri, P.; Koppens, F. H. L.; et al. *ACS Nano* **2019**, *13*, 8926–8935.
- (89) Miseikis, V.; Bianco, F.; David, J.; Gemmi, M.; Pellegrini, V.; Romagnoli, M.; Coletti, C. *2D Mater.* **2017**, *4*, 021004.
- (90) Li, X.; Magnuson, C. W.; Venugopal, A.; An, J.; Suk, J. W.; Han, B.; Borysiak, M.; Cai, W.; Velamakanni, A.; Zhu, Y.; et al. *Nano Lett.* **2010**, *10*, 4328–4334.
- (91) Wang, B.; Huang, M.; Tao, L.; Lee, S. H.; Jang, A.; Li, B.; Shin, H. S.; Akinwande, D.; Ruoff, R. S. *ACS Nano* **2016**, *10*, 1404–1410.
- (92) Suk, J. W.; Kitt, A.; Magnuson, C. W.; Hao, Y.; Ahmed, S.; An, J.; Swan, A. K.; Goldberg, B. B.; Ruoff, R. S. *ACS Nano* **2011**, *5*, 6916–6924.
- (93) Goykhman, I.; Desiatov, B.; Khurgin, J.; Shappir, J.; Levy, U. *Nano Lett.* **2011**, *11*, 2219–2224.
- (94) Goykhman, I.; Desiatov, B.; Khurgin, J.; Shappir, J.; Levy, U. *Opt. Express* **2012**, *20*, 28594–28602.
- (95) Echtermeyer, T. J.; Britnell, L.; Jasnos, P. K.; Lombardo, A.; Gorbachev, R. V.; Grigorenko, A. N.; Geim, A. K.; Ferrari, A. C.; Novoselov, K. S. *Nat. Commun.* **2011**, *2*, 455–458.
- (96) Fang, Z.; Liu, Z.; Wang, Y.; Ajayan, P. M.; Nordlander, P.; Halas, N. J. *Nano Lett.* **2012**, *12*, 3808–3813.
- (97) Echtermeyer, T. J.; Milana, S.; Sassi, U.; Eiden, A.; Wu, M.; Lidorikis, E.; Ferrari, A. C. *Nano Lett.* **2016**, *16*, 8–20.
- (98) Salamin, Y.; Heni, W.; Haffner, C.; Fedoryshyn, Y.; Hoessbacher, C.; Bonjour, R.; Zahner, M.; Hillerkuss, D.; Leuchtmann, P.; Elder, D. L.; et al. *Nano Lett.* **2015**, *15*, 8342–8346.
- (99) Salamin, Y.; Baeuerle, B.; Heni, W.; Abrecht, F. C.; Josten, A.; Fedoryshyn, Y.; Haffner, C.; Bonjour, R.; Watanabe, T.; Burla, M.; et al. *Nat. Photonics* **2018**, *12*, 749–753.
- (100) Chen, C.; Youngblood, N.; Peng, R.; Yoo, D.; Mohr, D. A.; Johnson, T. W.; Oh, S.; Li, M. *Nano Lett.* **2017**, *17*, 985–991.
- (101) Reed, G. T. *Silicon Photonics: The State of the Art*; John Wiley & Sons: Chichester, 2008.
- (102) Desiatov, B.; Goykhman, I.; Levy, U. *Nano Lett.* **2014**, *14*, 648–652.
- (103) Shin, W.; Raman, A.; Fan, S. J. *J. Opt. Soc. Am. B* **2012**, *29*, 1048–1054.
- (104) Novoselov, K. S.; Geim, A. K.; Morozov, S. V.; Jiang, D.; Zhang, Y.; Dubonos, S. V.; Grigorieva, I. V.; Firsov, A. A. *Science* **2004**, *306*, 666–669.
- (105) Senior, J. M.; Jamro, M. Y. *Optical fiber communications: principles and practice*; Pearson Education: Harlow, 2009.
- (106) Diels, J.; Rudolph, W. *Ultrashort laser pulse phenomena*; Elsevier: London, 2006.
- (107) Lagatsky, A.; Sun, Z.; Kulmala, T.; Sundaram, R.; Milana, S.; Torrisi, F.; Antipov, O.; Lee, Y.; Ahn, J.; Brown, C. *Appl. Phys. Lett.* **2013**, *102*, 013113.
- (108) Ferrari, A. C.; Meyer, J. C.; Scardaci, V.; Casiraghi, C.; Lazzeri, M.; Mauri, F.; Piscanec, S.; Jiang, D.; Novoselov, K. S.; Roth, S.; et al. *Phys. Rev. Lett.* **2006**, *97*, 187401.
- (109) Ferrari, A. C.; Basko, D. M. *Nat. Nanotechnol.* **2013**, *8*, 235–246.
- (110) Das, A.; Pisana, S.; Chakraborty, B.; Piscanec, S.; Saha, S. K.; Waghmare, U. V.; Novoselov, K. S.; Krishnamurthy, H. R.; Geim, A. K.; Ferrari, A. C.; et al. *Nat. Nanotechnol.* **2008**, *3*, 210–215.
- (111) Basko, D. M.; Piscanec, S.; Ferrari, A. C. *Phys. Rev. B* **2009**, *80*, 165413.
- (112) Emani, N. K.; Kildishev, A. V.; Shalae, V. M.; Boltasseva, A. *Nanophotonics* **2015**, *4*, 214–223.
- (113) Hanson, G. W. *J. Appl. Phys.* **2008**, *103*, 064302. *ibid.* **2013**, *113*, 029902.
- (114) Reed, G. T.; Knights, A. P. *Silicon Photonics: An Introduction*; John Wiley & Sons: Chichester, 2004.
- (115) Soavi, G.; Wang, G.; Rostami, H.; Purdie, D. G.; De Fazio, D.; Ma, T.; Luo, B.; Wang, J.; Ott, A. K.; Yoon, D.; et al. *Nat. Nanotechnol.* **2018**, *13*, 583–588.
- (116) Soavi, G.; Wang, G.; Rostami, H.; Tomadin, A.; Balci, O.; Paradeisanos, I.; Pogna, E.; Cerullo, G.; Lidorikis, E.; Polini, M. 2019, arXiv:1903.00989. ArXiv e-Print archive. <https://arxiv.org/abs/1903.00989>.
- (117) Tian, J.; Yu, S.; Yan, W.; Qiu, M. *Appl. Phys. Lett.* **2009**, *95*, 013504.
- (118) Dabos, G.; Ketzaki, D.; Manolis, A.; Chatzianagnostou, E.; Markey, L.; Weeber, J.; Dereux, A.; Giesecke, A. L.; Porschatis, C.; Chmielak, B.; et al. *IEEE Photon. J.* **2018**, *10*, 2700308.
- (119) Li, Q.; Qiu, M. *Opt. Express* **2010**, *18*, 15531–15543.
- (120) Delacour, C.; Blaize, S.; Grosse, P.; Fedeli, J. M.; Bruyant, A.; Salas-Montiel, R.; Lerondel, G.; Chelnokov, A. *Nano Lett.* **2010**, *10*, 2922–2926.